

# Simulating the H<sub>2</sub> content of high-redshift galaxies

Matteo Tomassetti <sup>\*</sup>, Cristiano Porciani, Emilio Romano-Diaz, Aaron D. Ludlow  
*Argelander Institut für Astronomie, Auf Dem Hügel 71, Bonn 53121, Germany*

Accepted 2014 ??? ?. Received 2014 ??? ?; in original form 2014 ??? ?

## ABSTRACT

We introduce a sub-grid model for the non-equilibrium abundance of molecular hydrogen in cosmological simulations of galaxy formation. We improve upon previous work by accounting for the unresolved structure of molecular clouds in a phenomenological way which combines both observational and numerical results on the properties of the turbulent interstellar medium. We apply the model to a cosmological simulation of the formation of a Milky-Way-sized galaxy at  $z = 2$ , and compare the results to those obtained using other popular prescriptions that compute the equilibrium abundance of H<sub>2</sub>. In these runs we introduce an explicit link between star formation and the local H<sub>2</sub> abundance, and perform an additional simulation in which star formation is linked directly to the density of cold gas. We find that, although the global properties of the simulated galaxy are relatively insensitive to the sub-grid H<sub>2</sub> models, the resulting spatial distribution of H<sub>2</sub> is not: molecules extend further into the outer disc of the galaxy in our non-equilibrium model. In addition, the destruction of molecules by supernovae, if substantial, may result in a depletion of the H<sub>2</sub> abundance in the innermost 2 – 3 kpc. Finally, we study dwarf-sized galaxies that lie in the high-resolution region of our simulations and show that their star formation histories are significantly affected by both early metal enrichment and numerical resolution. We conclude that further work is needed in order to verify recent claims on the abundance of dark galaxies at high redshift.

**Key words:**

## 1 INTRODUCTION

The process of galaxy formation involves the interplay of many non-linear phenomena that span a wide range of length and time scales. A galaxy like our Milky Way, for example, forms from a region that initially extends to roughly one comoving Mpc, yet its angular momentum is determined by the mass distribution within tens of comoving Mpc. Star formation, on the other hand, takes place in the densest cores of giant molecular clouds (GMCs), on scales of order of 0.1 pc.

The challenge in simulations of galaxy formation is to capture this vast dynamic range while simultaneously accounting for the different physical processes that intervene on relevant scales. This is usually achieved with *ad hoc* sub-grid models that attempt to emulate the most important small-scale phenomena. In particular, one of the biggest uncertainties in simulations of galaxy formation is the means

by which gas is converted into stars (see Dobbs et al. 2013, for a recent review).

The standard approach to this problem, motivated by observations, is to adopt a Schmidt-like law (Schmidt 1959), often coupled to conditions on the local gas properties. However, there are several issues with this method. First, its parameters are poorly constrained and are usually fine-tuned to match the observed Kennicutt-Schmidt (KS) relation (Kennicutt 1989, 1998). Second, there is a growing body of evidence that the local star formation rate correlates more tightly with the observed density of molecular hydrogen than with that of the total gas density (e.g. Kennicutt et al. 2007; Bigiel et al. 2008; Leroy et al. 2008), though there is yet no consensus as to whether this reflects a causal relation. In particular, numerical simulations of isolated molecular clouds suggest that the presence of molecules does not boost the ability of the gas to cool and form stars (Glover & Clark 2012). The tight spatial correlation between H<sub>2</sub> and young stars may then be due to the fact that they are both formed in high density regions where gas is effectively shielded from the interstellar radiation field.

Despite the ongoing debate, there are strong motivations for including a treatment of molecular hydrogen in

<sup>\*</sup> E-mail: mtomas@astro.uni-bonn.de

Member of the International Max Planck Research School (IMPRS) for Astronomy and Astrophysics at the Universities of Bonn and Cologne

cosmological simulations of galaxy formation. Observations of  $\text{H}_2$  proxies (such as CO luminosity), for example, have progressed tremendously over the past decade (see Carilli & Walter 2013, for a recent review), underlining the need for robust theoretical templates to aid in the design of observational campaigns and the interpretation of their results. Furthermore, numerical simulations constitute a unique tool to test the impact of  $\text{H}_2$ -regulated star formation on the global structure of galaxies, provided their  $\text{H}_2$  content can be reliably determined.

Tracking  $\text{H}_2$ , however, requires solving a challenging network of rate equations which are coupled to a radiative-transfer computation for  $\text{H}_2$ -dissociating photons. Given that the spatial resolution of current simulations is comparable in size to GMCs, these calculations must be done at the sub-grid level and include a description of gas structure on the unresolved scales (e.g. a clumping factor for the gas density).

Recently, several authors have incorporated simple algorithms to track molecular hydrogen in hydrodynamical simulations of galaxy formation. For instance, Pelupessy et al. (2006) monitored the  $\text{H}_2$  distribution in dwarf-sized galaxies within a fixed dark-matter potential and showed that the resulting molecular mass depends strongly on the metallicity of the interstellar medium (ISM). Similar conclusions were drawn by Gnedin et al. (2009, see also Feldmann et al. (2011)), who followed the evolution of the  $\text{H}_2$  content for 100 Myr in a cosmologically simulated galaxy at  $z = 4$ . These authors showed that it is only possible to form fully shielded molecular clouds when the gas metallicity is high (i.e.  $Z \sim 10^{-2} - 10^{-1} Z_\odot$ ), and argued that  $\text{H}_2$ -regulated star formation can act as an effective feedback mechanism, delaying star formation in the low-metallicity progenitors of a galaxy.

The implications of these results for galaxy formation in low-mass halos was studied further by Kuhlen et al. (2012, 2013), who suggested the possible existence of a large population of low-mass, gas-rich galaxies that never reached the critical column density required for the  $\text{H}_2/\text{HI}$  transition and are thus devoid of stars. Their work, however, was based on an analytic model for  $\text{H}_2$  formation that assumes chemical equilibrium between its formation and destruction rates (Krumholz et al. 2008, 2009; McKee & Krumholz 2010). None the less, Krumholz & Gnedin (2011) showed that this model agrees well with a time-dependent solution to the chemical network provided the local metallicity of the gas is above  $10^{-2} Z_\odot$ , lending support to these conclusions.

Christensen et al. (2012) modeled the non-equilibrium abundance of  $\text{H}_2$  in a dwarf galaxy that was simulated down to redshift  $z = 0$ , connecting star formation explicitly to the local  $\text{H}_2$  content of the gas. These authors showed that, compared to simulations rooted on the Schmidt law, molecule-based star formation produces a galaxy which is more gas rich, has bluer stellar populations and a clumpier ISM. On the other hand, strong stellar feedback, when included, tends to mitigate these differences by regulating the formation and destruction rates of GMCs (Hopkins et al. 2012).

In this paper, we introduce a new time-dependent sub-grid model for tracking the non-equilibrium abundance of  $\text{H}_2$  in cosmological simulations of galaxy assembly. Our approach builds upon the work of Gnedin et al. (2009) and Christensen et al. (2012) by including additional informa-

tion on the unresolved distribution of gas temperatures and densities. In particular, our model: i) explicitly accounts for the distribution of sub-grid densities, as determined by observations and numerical simulations of turbulent GMCs; ii) invokes a gas temperature-density relation that was determined from detailed numerical studies of the ISM (Glover & Mac Low 2007a); and iii) consistently takes into account that denser, unresolved clumps have larger optical depths.

As an application, we employ the model in a high-resolution simulation that follows the formation of a Milky-Way-sized galaxy down to  $z = 2$ . In order to explore the interplay between star formation,  $\text{H}_2$  abundance and galactic structure, we re-simulate the same volume using different algorithms for computing the density of molecular hydrogen and the local star formation rate.

The paper is organized as follows. In Section 2, we introduce our model for tracking the non-equilibrium  $\text{H}_2$  abundance and compare it with other commonly adopted prescriptions that have been discussed in the literature. In Sections 3 and 4, we describe our suite of simulations and present our main results. Finally, we summarize our main conclusions and then critically discuss some of our assumptions in Section 5.

## 2 MOLECULAR HYDROGEN

The abundance of molecular hydrogen in the metal-rich ISM is mainly regulated by the competition between its formation due to the catalytic action of dust grains and its photo-dissociation via the two-step Solomon process. In the ground state,  $\text{H}_2$  absorbs electromagnetic radiation in two densely packed series of lines (the Lyman band – characterized by photon energies  $E > 11.2$  eV or wavelengths  $\lambda < 1108 \text{ \AA}$  – and the Werner band –  $E > 12.3$  eV,  $\lambda < 1008 \text{ \AA}$ ). Radiative decay from the excited states leads to dissociation in approximately 15 per cent of the cases. Direct photo-dissociation would require photons with energy  $E > 14.7$  eV, but these are principally absorbed by hydrogen atoms as they lie above the hydrogen photo-ionization threshold (13.6 eV, 912  $\text{\AA}$ ). As a result, only photons between  $912 \text{ \AA} < \lambda < 1108 \text{ \AA}$  can photo-dissociate molecular hydrogen.

Lyman-Werner (LW) photons are copiously emitted by OB stars, but intervening  $\text{H}_2$  and dust effectively shield the densest regions of the ISM. This results in an  $\text{H}_2$  abundance that increases rapidly toward regions in which the medium becomes optically thick to LW radiation.

An exact treatment of these effects is challenging: it requires three-dimensional radiative transfer calculations capable of resolving length and time-scales orders of magnitude shorter than those associated with galaxy evolution. Nevertheless, it is possible to follow the formation of molecular complexes in a phenomenological way, using approximate sub-grid treatments of the most crucial physical processes involved.

In this work, we use three different mathematical models that attempt to approximate these effects. The simplest (KMT-EQ) is fully analytical; it returns the equilibrium  $\text{H}_2$  fraction in terms of quantities that can be determined locally in a simulation (Krumholz et al. 2008, 2009; McKee & Krumholz 2010). The model is based on a spherical molecular complex immersed in an isotropic bath of LW photons.

Assuming that the ISM is in a two-phase equilibrium between a cold and a warm neutral medium, it allows both the intensity of the radiation field and the resulting  $H_2$  fraction to be expressed in terms of the local gas column density and metallicity (Krumholz & Gnedin 2011).

The second model (KMT-UV) employs the same analytical relation between the equilibrium  $H_2$  fraction and the radiation density in the LW band. However, in this case, the latter is calculated numerically within the simulations themselves. This is achieved by propagating photons from stellar particles assuming that the ISM is optically thin within a characteristic length scale and optically thick beyond that (see Appendix A for further details).

Note, however, that the formation of molecular hydrogen on dust grains is a very inefficient process. In the metal poor ISM, for example, the  $H_2$  formation timescale approaches a Hubble time. This calls into question the appropriateness of the equilibrium-based models, which *instantaneously* populate each simulation volume element with a given fraction of  $H_2$ . This has motivated several authors (Pelupessy et al. 2006; Gnedin et al. 2009; Christensen et al. 2012) to develop more sophisticated algorithms capable of tracking the non-equilibrium  $H_2$  fraction in high-resolution simulations. Inspired by these efforts, we have developed a novel dynamical model (DYN) for calculating the abundance of molecular hydrogen. This model is described in detail in the following subsection.

## 2.1 Mathematical formulation of the model

The evolution of the  $H_2$  number density is described by the following system of equations:

$$\frac{dn_{H_2}}{dt} = \mathcal{R}_f(T) n_{HI} n_H - G \kappa \Phi e^{-\tau} n_{H_2} + \quad (1)$$

$$- \gamma_{HI} n_{HI} n_{H_2} - \gamma_{H_2} n_{H_2}^2,$$

$$\frac{dn_{HI}}{dt} = n_e n_{HI} k_1(T) + \quad (2)$$

$$- n_{HI} [k_2(T) n_e + \Gamma(z)] - 2 \frac{dn_{H_2}}{dt},$$

$$n_{HI} + n_{HII} + 2n_{H_2} = n_H. \quad (3)$$

Here  $n_{HI}$ ,  $n_{HII}$  and  $n_{H_2}$  are, respectively, the number densities of neutral, ionized and molecular hydrogen;  $n_e$  is the electron number density;  $\gamma_i$  is the  $H_2$  collisional destruction rate due to interaction with species  $i$ ;  $G$  is the unshielded interstellar UV-radiation flux in Habing units ( $G_0 = 1.6 \times 10^{-3}$  erg cm $^{-2}$  s $^{-1}$ );  $\kappa$  is the  $H_2$  photo-dissociation rate for  $G = 1$ ;  $\Gamma(z)$  is the photo-ionization rate<sup>1</sup> of HI;  $k_1$  and  $k_2$  are the hydrogen recombination and collisional destruction rates;  $\tau = \sigma_d N_H$  is the optical depth of dust in the LW bands (conventionally evaluated at 1000 Å), where  $N_H$  is the total hydrogen column density. This assumes that the dust abundance scales linearly with the gas metallicity and the dust-to-gas mass ratio is equal to the value measured in the MW, i.e.  $10^{-1} Z/Z_\odot$ . The parameterization of the  $H_2$  self-shielding function,  $\Phi$  (approximated for the plane parallel

case) and the  $H_2$  formation rate on dust grains,  $\mathcal{R}_f$ , are given in Table 1, and adopt a dust temperature  $T_d = 10$  K.

### 2.1.1 Accounting for unresolved structures

Cosmological simulations of galaxy formation are limited in spatial resolution, and even the highest resolution runs employ computational elements that extend for a only few tens of parsecs. Observations and numerical studies of the turbulent ISM, on the other hand, reveal a complex gas density distribution on much smaller scales, consisting of filamentary structures and clumps (e.g. Glover & Mac Low 2007a). This structure is normally approximated in cosmological simulations by introducing a density clumping factor,  $C_\rho$ . However, as already noted by Micic et al. (2012), this does not take into account the full distribution of sub-grid densities, nor the effective density-temperature relation, both of which may modify the sub-grid  $H_2$  formation and destruction rates.

Motivated by observations of the GMC density distribution (e.g. Kainulainen et al. 2009; Schneider et al. 2013), we assume that sub-grid clumps follow a log-normal (mass-weighted) probability density function (PDF):

$$\mathcal{P}_M dn_H = \frac{1}{\sqrt{2\pi}\sigma n_H} e^{-\frac{(\ln n_H - \mu)^2}{2\sigma^2}} dn_H, \quad (4)$$

where  $\mu$  and  $\sigma$  are parameters that can be determined once a clumping factor has been chosen. To do so, note that the average hydrogen density within a computational volume element,  $\langle n_H \rangle$ , is simply the integral over the volume-weighted sub-grid density PDF,  $\mathcal{P}_V$ :

$$\langle n_H \rangle = \frac{\int_0^\infty dn_H n_H \mathcal{P}_V}{\int_0^\infty dn_H \mathcal{P}_V} = e^{\mu+3/2\sigma^2}, \quad (5)$$

where the last expression derives from the fact that  $\mathcal{P}_V/\mathcal{P}_M = dM/dV = n_H$ . Similarly,  $C_\rho \equiv \langle n_H^2 \rangle / \langle n_H \rangle^2 = e^{\sigma^2}$ , so that the sub-grid density PDF is fully determined by  $C_\rho$  and the total hydrogen density in a cell.

In principle,  $C_\rho$  is a local variable whose value depends on the turbulent velocity dispersion of the ISM (e.g. Price et al. 2011). However, for simplicity, and in order to facilitate comparison with previous work, we set  $C_\rho = 10$  which has been shown to reproduce observed  $H_2$  fractions in nearby galaxies (e.g. Gnedin et al. 2009; Christensen et al. 2012).

We assume that unresolved gas concentrations follow a temperature-density relation that emerges from simulations of the turbulent ISM (see Figure 17 in Glover & Mac Low 2007b). These results suggest that, at the densities relevant for efficient  $H_2$  formation, gas temperatures rarely exceed 200 K. We therefore assume that atomic hydrogen and helium remain neutral within each cell, and neglect the collisional terms in equations (1) and (2). The resulting equations can then be rewritten

$$\frac{d\langle n_{H_2} \rangle}{dt} = \langle \mathcal{R}_f(T) n_{HI} n_H \rangle - \langle G \kappa \Phi e^{-\tau} n_{H_2} \rangle, \quad (6)$$

$$\frac{d\langle n_{HI} \rangle}{dt} = -2 \frac{d\langle n_{H_2} \rangle}{dt}, \quad (7)$$

$$\langle n_{HI} \rangle + 2\langle n_{H_2} \rangle = \langle n_H \rangle. \quad (8)$$

<sup>1</sup> In terms of the UV-background intensity,  $J_\nu$ , the ionization cross-section  $\sigma$  and the corresponding optical depth  $\tau'$ ,  $\Gamma(z) = \int_{\nu_0}^{+\infty} 4\pi J(\nu, z) \sigma(\nu) e^{-\tau'(\nu)} / (h\nu) d\nu$ , where  $\nu_0 = 13.6$  eV/ $h\nu$  and  $h\nu$  denotes the Planck constant.

Parameter	Symbol	Expression	Reference
Clumping factor	$C_\rho$	$\langle n_{\text{H}}^2 \rangle / \langle n_{\text{H}} \rangle^2 = 10$	1,2
H <sub>2</sub> formation rate on dust grains	$\mathcal{R}_f(T)$	$3.025 \times 10^{-17} S_{\text{H}}(T) (T/100 \text{ K})^{0.5} (Z/Z_\odot)$	5,6
Sticking probability for H atoms	$S_{\text{H}}(T)$	$\left[ 1 + 0.4 \left( \frac{T+T_d}{100 \text{ K}} \right)^{1/2} 0.2 \left( \frac{T}{100 \text{ K}} \right) + 0.08 \left( \frac{T}{100 \text{ K}} \right)^2 \right]^{-1}$ , $T_d = 10 \text{ K}$	3,4
H <sub>2</sub> photo-dissociation rate	$\kappa$	$3 \times 10^{-11} \text{ s}^{-1}$	7
Self-shielding function	$\Phi$	$\frac{\omega}{(1+x/b_5)^2} + \frac{1-\omega}{(1+x)^{1/2}} \exp[-8.5 \times 10^{-4}(1+x)^{1/2}]$ $x = N_{\text{H}_2}/5 \times 10^{14} \text{ cm}^{-2}$ , $\omega = 0.035$ , $b_5 = 7.1$	8,9
Cross-section at 1000 Å	$\sigma_d$	$2 \times 10^{-21} (Z/Z_\odot) \text{ cm}^{-2}$	8

*References:*

1: Gnedin et al. (2009) 2: Christensen et al. (2012), 3: Cazaux & Spaans (2009), 4: Burke & Hollenbach (1983), 5: Tielens & Hollenbach (1985), 6: Cazaux & Spaans (2004), 7: Glover & Mac Low (2007a), 8: Draine & Bertoldi (1996), 9: Krumholz (2012)

**Table 1.** Parameters of the non-equilibrium model for the H<sub>2</sub> abundance.

### 2.1.2 Solving the differential equations

Given our assumptions for the sub-grid density and temperature distributions, the above rate equations are exact. However, it is impractical to preserve the information about the abundance of molecular hydrogen at each sub-grid density between time-steps, and further simplifications are needed. We therefore assume that, within a computational cell, atomic gas transitions to a fully molecular state above a critical (sub-grid) density threshold,  $n_c$ . With this, equation (6) reduces to

$$\frac{d\langle n_{\text{H}_2} \rangle}{dt} = \frac{C_\rho}{\langle n_{\text{H}} \rangle} \left( \int_0^{n_c} dn \mathcal{R}_f[T(n)] n^3 \mathcal{P}_M + \right. \quad (9)$$

$$\left. - \frac{\langle G \rangle \kappa}{2} \int_{n_c}^{+\infty} dn \Phi(n) e^{-\tau(n)} n^2 \mathcal{P}_M \right).$$

Note that, for a log-normal probability distribution of densities,  $n_c$  can be obtained solving for the root of

$$\langle n_{\text{H}_2} \rangle = \frac{\langle n_{\text{H}} \rangle}{4} \left[ 1 + \text{Erf} \left( \frac{\mu + 2\sigma^2 - \ln(n_c)}{\sqrt{2}\sigma} \right) \right]. \quad (10)$$

At each time step of the simulation, we solve equation (9) in relevant cells using a variable step-size, variable order, implicit integrator. Using this we determine the *total* H<sub>2</sub> density per cell, which we advect with the gas flow at each timestep.

### 2.1.3 Estimating optical depths

In order to evaluate equation (9), the dust optical depth,  $\tau(n)$ , and H<sub>2</sub> column density (which is necessary to compute the self-shielding function,  $\Phi$ ) must be specified. We derive estimates for these quantities as follows. First, working at the grid level, we compute column densities (surface densities in case of the KMT model) by means of a Sobolev-like approximation

$$N_{\text{H}} \approx \langle n_{\text{H}} \rangle \times l_{\text{sob}}, \quad \Sigma_{\text{gas}} \approx \langle \rho_{\text{gas}} \rangle \times l_{\text{sob}}, \quad (11)$$

where  $l_{\text{sob}} = \langle n_{\text{H}} \rangle / |\nabla \langle n_{\text{H}} \rangle|$ , and  $\rho_{\text{gas}}$  is the total gas density. This is a reasonable approximation in simulations where computational elements are of comparable extension to the sizes of GMCs (Gnedin et al. 2009; Kuhlen et al. 2012; Christensen et al. 2012).

On sub-grid scales,  $\tau(n)$  depends on the *unresolved* density distribution, rather than on the mean cell density,  $\langle n_{\text{H}} \rangle$ .

We therefore approximate the density-dependence of the dust optical depth in two regimes. For  $n_{\text{H}} < \langle n_{\text{H}} \rangle$ , we assume that  $\tau$  is given by the average optical depth of the macroscopic cell,  $\langle \tau \rangle$ . For  $n_{\text{H}} > \langle n_{\text{H}} \rangle$ , we boost  $\tau$  within GMCs by approximating their radial density profiles using a power-law,  $n_{\text{H}}(r) = A r^{-2}$  (e.g. Pirogov 2009; Schneider et al. 2013). Note that the normalization constant  $A$  depends on the detailed structure of the clumps. For simplicity, we assume  $A \approx 3 \times 10^{40} \text{ cm}^{-1}$ , consistent with a typical GMC of mass  $M_c = 10^5 M_\odot$  and radius  $R_c = 100 \text{ pc}$ . Given these assumptions, we can express the (sub-grid) optical depth as

$$\tau(n) = \langle \tau \rangle + \begin{cases} 0, & n_{\text{H}} < \langle n_{\text{H}} \rangle \\ \sqrt{A} \sigma_d (n_{\text{H}}^{1/2} - \langle n_{\text{H}} \rangle^{1/2}), & n_{\text{H}} > \langle n_{\text{H}} \rangle. \end{cases} \quad (12)$$

Similarly, when computing H<sub>2</sub> column densities we add an extra contribution from the sub-grid densities that are fully molecular, resulting in

$$N_{\text{H}_2} = \langle N_{\text{H}_2} \rangle + \begin{cases} 0, & n_{\text{H}} < n_c \\ \frac{\sqrt{A}}{2} (n_{\text{H}}^{1/2} - n_c^{1/2}), & n_{\text{H}} > n_c, \end{cases} \quad (13)$$

where we have used  $n_{\text{H}_2}(r) = n_{\text{H}}(r)/2$  for  $n_{\text{H}} > n_c$ .

### 2.1.4 Example solutions

To develop an intuitive understanding of the impact of our sub-grid density distribution on H<sub>2</sub> formation, we integrate the rate equations for 500 Myr and compute the H<sub>2</sub> content for cells of fixed density and metallicity in a constant UV field. The results are shown in Figure 1, where curves correspond to  $\langle f_{\text{H}_2} \rangle = 2\langle n_{\text{H}_2} \rangle / \langle n_{\text{H}} \rangle = 0.5$  in the  $(\langle n_{\text{H}} \rangle, \langle G \rangle)$  plane for gas metallicities ranging from  $10^{-3} Z_\odot$  to  $10 Z_\odot$ . As expected, higher metallicity gas forms H<sub>2</sub> more efficiently at low densities. This is due to the enhanced rate of H<sub>2</sub> formation on dust grains, but also to the increased optical depth to LW photons (see equation (12)). More importantly, note that the H<sub>2</sub> fraction is nearly independent of  $\langle G \rangle$ , suggesting that our results will not be strongly influenced by our treatment of the UV field.

## 2.2 A Comparison of H<sub>2</sub> Formation Models

In Figure 2 we compare the predictions of the three H<sub>2</sub>-formation models described above (KMT-EQ, KMT-UV

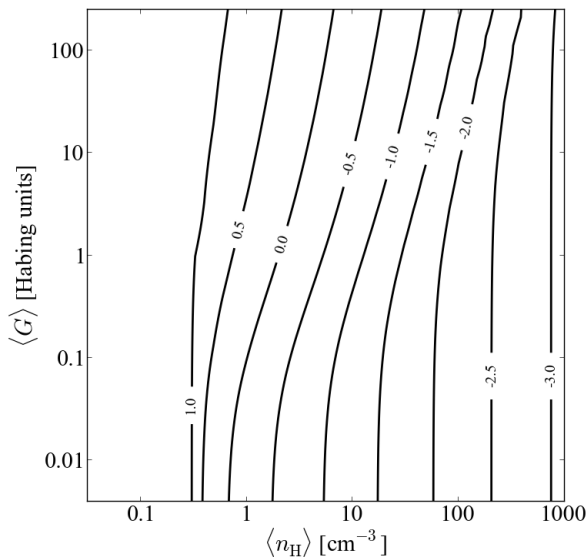


**Figure 1.** Lines of constant  $\langle f_{H_2} \rangle = 0.5$  as a function of the total hydrogen density,  $\langle n_H \rangle$ , and the interstellar UV field,  $\langle G \rangle$ , for the DYN model after an integration time of 500 Myr. Labels along each curve indicate the logarithm of the gas metallicity in solar units.

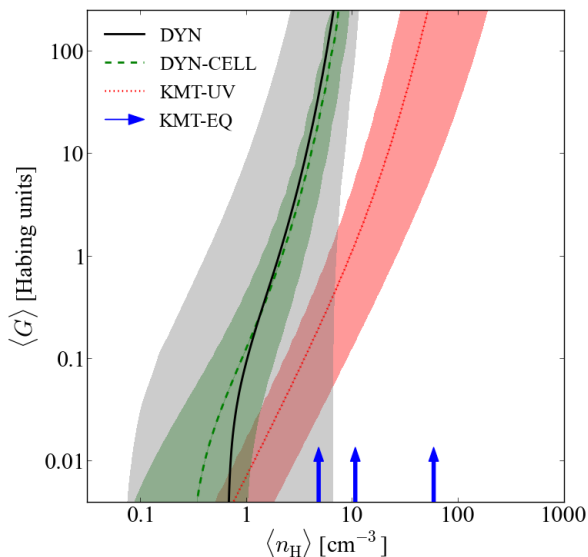


**Figure 2.** Lines correspond to contours of  $\langle f_{H_2} \rangle = 0.5$  for a solar metallicity gas. Different linestyles correspond to the different  $H_2$  formation models described in Section 2, as indicated in the legend. The dashed (green) line, labeled DYN-CELL, shows the results of the DYN model in which sub-grid densities are accounted for using a clumping factor rather than a sub-grid density PDF. Shaded regions of similar color highlight the zone  $0.1 < \langle f_{H_2} \rangle < 0.9$  for each model. Upward pointing arrows mark  $\langle f_{H_2} \rangle = 0.1, 0.5$  and  $0.9$  (from left to right) for KMT-EQ, which is independent of  $\langle G \rangle$ . For the non-equilibrium models the solution has been computed after a total integration time of 500 Myr.

and DYN). Lines show contours of  $\langle f_{H_2} \rangle = 0.5$  in the plane of UV field and gas density for a solar metallicity gas; shaded regions indicate the range  $0.1 < \langle f_{H_2} \rangle < 0.9$ . Different line styles correspond to the different models: DYN (solid), KMT-UV (dotted), and upward pointing arrows mark  $\langle f_{H_2} \rangle = 0.1, 0.5$  and  $0.9$  (from left to right) for KMT-EQ (which, by construction, is independent of  $\langle G \rangle$ ).

We also show, using a dashed (green) line, the time-dependent solution obtained after multiplying all quadratic terms by  $C_p = 10$  but without integrating over the sub-grid density PDF. This approximation (labeled DYN-CELL) has been used in previous work (Gnedin et al. 2009; Christensen et al. 2012), and is shown here for comparison. In this case we set a constant gas temperature of  $T = 10^3$  K, which is typical of star forming cells in simulations of galaxy formation. The solutions for all time-dependent models have been integrated for 500 Myr. Note that within this time, gas densities  $n_H \gtrsim 1 \text{ cm}^{-3}$  have reached equilibrium and a longer integration times would only impact the very low density regions, without altering our conclusions.

It is worth noting that the DYN and DYN-CELL models have very similar contours at  $\langle f_{H_2} \rangle = 0.5$  over roughly five orders of magnitude in UV field. The  $\langle f_{H_2} \rangle = 0.1$  and  $0.9$  contours, on the other hand, differ dramatically. For example, for  $\langle G \rangle = 1$ , the DYN model reaches an  $H_2$  fraction of  $0.9$  at  $n_H \sim 5 \text{ cm}^{-3}$ , which is a factor of 5 larger than the DYN-CELL model. This results from the sub-grid temperature-density relation in the DYN model: dense clumps, in this case, are very cold, which inhibits the efficient formation of  $H_2$  on dust grains. For example, at  $n_H \gtrsim 10^2 \text{ cm}^{-3}$  sub-grid clumps have  $T \lesssim 10^2$  K. Since the  $H_2$  formation rate,  $\mathcal{R}_f$ , is proportional to  $\sqrt{T} S_H(T)$ , this results in lower  $\langle f_{H_2} \rangle$  than for the DYN-CELL model, where  $T = 10^3$  K everywhere.

However, for the same value of  $\langle G \rangle$ ,  $\langle f_{H_2} \rangle = 0.1$  is reached at much lower densities in the DYN model. In this regime, the temperature does not strongly affect the  $H_2$  formation rate. The difference, in this case, is due to the integration over the sub-grid densities, which enhances shielding from LW photons resulting in higher  $H_2$  abundances.

For solar metallicity, the KMT-UV and KMT-EQ models predict a considerably lower  $H_2$  fraction than the time-dependent solutions. Simulations of galaxy formation that tie star formation directly to the  $H_2$  content of a given cell may therefore be affected by differing treatments of  $H_2$  formation on sub-grid scales. In order to test the impact of these assumptions, we have used each model described above to simulate the formation of a massive galaxy at  $z = 2$ . These simulations are described below.

### 3 NUMERICAL SIMULATIONS

#### 3.1 Simulation setup

We ran several cosmological simulations of the formation of a massive ( $\sim 10^{12} h^{-1} M_\odot$ ) galaxy up to redshift  $z_f = 2$  using the fully Eulerian code RAMSES (Teyssier 2002). Each simulation started from the same initial conditions but employed different models for  $H_2$  and star formation, as detailed below (see Table 2 for a compact summary of our runs).

Run	H <sub>2</sub> model	$\dot{\rho}_{\text{SF}} \propto \langle \rho_i \rangle$	SNe destroy H <sub>2</sub>	$\ell_i$	$\ell_f$	$\Delta x$ ( $h^{-1}$ pc)	$z_i$	$z_f$
STD	KMT-UV	gas	-	11	17	130	99	2
DYN	DYN	H <sub>2</sub>	✓	11	17	130	99	2
DYN-B	DYN	H <sub>2</sub>	-	11	17	130	99	3
DYN-HR	DYN	H <sub>2</sub>	✓	12	18	65	99	4
KMT-EQ	KMT-EQ	H <sub>2</sub>	-	11	17	130	99	2
KMT-UV	KMT-UV	H <sub>2</sub>	-	11	17	130	99	2

**Table 2.** Simulations used in this work. Symbols are defined in the main text.

### 3.1.1 Cosmological model

Each run adopted a flat  $\Lambda$ CDM cosmological model consistent with the WMAP 7-year data release (Komatsu et al. 2011). The corresponding parameters are:  $\Omega_m = 0.2726$ ,  $\Omega_b = 0.0456$ ,  $\sigma_8 = 0.809$ ,  $n_s = 0.963$  and  $h = 0.704$ . Here  $\Omega_m$  and  $\Omega_b$  denote the current density parameters for the total matter and the baryonic component, respectively;  $\sigma_8$  is the rms mass fluctuation in  $8 h^{-1}$  Mpc spheres, linearly extrapolated to  $z = 0$ ;  $n_s$  is the spectral index of the primordial density fluctuation spectrum, and  $h$  is the Hubble parameter expressed in units of  $100 \text{ km s}^{-1} \text{ Mpc}^{-1}$ .

### 3.1.2 Initial conditions

Initial conditions for our simulations were generated with the MUSIC code (Hahn & Abel 2011) in the following way. We first ran a collisionless “parent” simulation of a  $50 h^{-1}$  Mpc box from  $z_i = 99$  to  $z_f = 0$ . From the  $z = 2$  output, we randomly selected a dark matter halo with an approximate virial mass<sup>2</sup>  $M_{200} \sim 10^{12} h^{-1} M_\odot$  that also had a quiescent late-time accretion history. All particles within  $3 \times r_{200}$  (at  $z = 0$ , when the halo has a mass  $M_{200} \simeq 3 \times 10^{12} h^{-1} M_\odot$ ) were then traced back to the unperturbed linear density field and the comoving volume enclosing these particles ( $\sim (7 h^{-1} \text{ Mpc})^3$ ) was resampled at higher resolution in both dark matter and gas. The global setup includes several nested levels of refinement and periodic boundary conditions.

For our suite of simulations, Lagrangian volume elements within the high-resolution region have a length-scale of  $\sim 24.4 h^{-1}$  comoving kpc. This is equivalent to resampling the entire initial  $50 h^{-1}$  Mpc simulation volume with  $2048^3$  cells ( $2^{3\ell_i}$  with  $\ell_i = 11$ ).

In addition to these runs, we have also carried out one simulation improving the linear spatial resolution by a factor of two. Because of computational restrictions, however, this run was only carried out to  $z_f = 4$ . For our cosmological parameters and box size, the dark matter particle masses in these runs are  $m_{\text{DM}} = 9.15 \times 10^5 h^{-1} M_\odot$  and  $m_{\text{DM}} = 1.14 \times 10^5 h^{-1} M_\odot$  in the low and high resolution cases, respectively.

<sup>2</sup> We define the halo mass,  $M_{200}$ , as that within a sphere of radius  $r_{200}$  that encloses a mean density equal to 200 times the critical density for closure,  $\rho_c = 3H_0^2/8\pi G_N$  (where  $G_N$  is the gravitational constant).

### 3.1.3 Numerical evolution

Each simulation was run using a version of the RAMSES code that was modified to include the various treatments of H<sub>2</sub> physics described in Section 2, as well as a new star formation routine. RAMSES is an AMR code which uses a second-order Godunov scheme to solve the hydrodynamic equations, while trajectories of stellar and dark-matter particles are computed using a multi-grid Particle-Mesh solver. Between redshifts  $z = 9$  and 2, we output 140 simulation snapshots, equally spaced in 20 Myr intervals.

The AMR technique superimposes finer sub-grids onto the multi-level mesh used to generate the initial conditions, resulting in finer resolution in high density regions. We employ a refinement strategy based on the standard “quasi-Lagrangian” criterion: a cell is split if it contains more than 8 dark-matter particles or a baryonic mass greater than  $8 m_{\text{DM}} \Omega_b / (\Omega_m - \Omega_b)$ . To prevent catastrophic refinement, we enforce a constant physical resolution and match the maximum AMR-level to that attained in a pure DM-run, as discussed in Section A8 of Scannapieco et al. (2012). This results in 6 additional levels of refinement before  $z_f$ , corresponding to a maximum level of  $\ell_f = 17$  (or 18 in the highest resolution case), and to a spatial resolution of  $130 h^{-1}$  pc ( $65 h^{-1}$  pc) at  $z = 2$ .

For the gas component, we assume an equation of state with polytropic index  $\gamma = 5/3$  and, to avoid spurious fragmentation, add thermal pressure using:  $\langle T \rangle = T_J (\langle n_H \rangle / n_J)^\gamma$ . Requiring the Jeans length to be resolved with at least four resolution elements (Truelove et al. 1997) one finds  $T_J \simeq 2500 (\Delta x / 130 h^{-1} \text{ pc})^{2/3}$  and  $n_J \simeq 3.8 (\Delta x / 130 h^{-1} \text{ pc})^{-4/3}$  for the Jeans temperature and density, where  $\Delta x$  is the (physical) length of the resolution element (Teyssier et al. 2010).

Our runs include star formation, supernova feedback and associated metal enrichment, as well as cooling from H, He and metals. We adopt the uniform cosmic UV background of Haardt & Madau (2012) and approximate self-shielding of dense gas by exponentially suppressing it in cells where the gas density exceeds  $\langle n_H \rangle \sim 0.014 \text{ cm}^{-3}$  (Tajiri & Umemura 1998). In addition, we approximately account for interstellar LW radiation in order to solve for the abundance of molecular hydrogen (see Appendix A, for further details).

## 3.2 Star Formation

Cosmological simulations of galaxy formation lack the spatial resolution required to model the cold ISM. Star formation is therefore implemented stochastically by converting gas mass elements into star particles provided that certain physical conditions are satisfied. The prevailing approach is

to relate the star formation-rate density,  $\dot{\rho}_{\text{SF}}$ , to the total local gas density in a cell,  $\langle \rho_{\text{gas}} \rangle$  and a suitable timescale,  $t_*$ , over which star formation is expected to take place (Schmidt 1959). One common prescription is given by

$$\dot{\rho}_{\text{SF}} = \varepsilon \frac{\langle \rho_{\text{gas}} \rangle}{t_*}, \quad (14)$$

where  $t_*$  is the free-fall time of the gas,  $t_{\text{ff}} = \sqrt{3\pi/(32G_N \langle \rho_{\text{gas}} \rangle)}$  and  $\varepsilon$  is an efficiency parameter.

Our “standard” run (STD) adopts this star formation law within cells above a critical density,  $n_*$ , and below a temperature threshold,  $T_c$ . We set  $T_c = 10^4$  K, and tune  $\varepsilon$  and  $\langle n_* \rangle$  in order to match the observed KS relation. This gives  $\langle n_* \rangle = 2/3 n_J$  and  $\varepsilon = 0.05$  which, in our 2048<sup>3</sup>-equivalent run, corresponds to a star formation density threshold of  $\langle n_* \rangle \simeq 2.5 \text{ cm}^{-3}$ . Note that, in our STD run, we also compute the local  $H_2$  abundance in post processing using the KMT-UV model.

Alternatively, star formation can be linked directly to the local density of molecular hydrogen (Pelupessy et al. 2006; Gnedin et al. 2009; Christensen et al. 2012; Kuhlen et al. 2012, 2013):

$$\dot{\rho}_{\text{SF}} = \varepsilon \frac{\langle \rho_{H_2} \rangle}{t_*}. \quad (15)$$

Note that this does not require a density threshold, which arises naturally in the equations regulating the abundance of  $H_2$  (see Figure 1): low density regions, where  $H_2$  formation is inefficient, are ineligible to form stars. Assuming that star formation takes place exclusively within GMCs, whose typical densities are of the order of  $100 \text{ cm}^{-3}$ , we set  $t_*$  in equation (15) to be the minimum of the free-fall time scales computed at the cell density and at  $100 \text{ cm}^{-3}$  (see also, Gnedin et al. 2009), and adopt  $\varepsilon = 0.05$ , as assumed for the STD run. Finally, in the DYN model, we only allow star formation if the temperature of a cell is below  $10^4$  K.

### 3.3 Feedback, metal enrichment and molecules

Massive stars end their lives as type II supernovae (SNe) which inject metals and energy into the ISM. Our runs adopt a stellar metallicity yield and a SNa return fraction consistent with a Kroupa (2001) initial mass function. We assume that each massive star releases  $10^{50} \text{ erg M}_{\odot}^{-1}$  of thermal energy into the ISM 10 Myr after their creation. To approximate the adiabatic expansion that follows a SNa explosion, we turn off gas cooling for the next 40 Myr in the affected cells (e.g. Stinson et al. 2006; Agertz et al. 2013).

The impact of SNe on the distribution of  $H_2$  on  $\sim 100$  pc scales is far from certain, and current simulations of the ISM reach conflicting results. Some authors find that  $H_2$  is almost completely destroyed (Stefanie Walch, personal communication) while others find that it quickly reforms due to the short cooling times of the densest regions (Rogers & Pittard 2013). We have bracketed this uncertainty by considering two extreme cases in our DYN model. In one, we reduced the  $H_2$  fraction to 10 per cent of its initial value in the cells that are directly influenced by SNe (i.e. those where the cooling is switched off). In a second simulation (run up to  $z_f = 3$ ), we leave the  $H_2$  distribution computed according to our non-equilibrium model unchanged in cells that have experienced recent SNe (we will refer to this run as DYN-B).

No  $H_2$  destruction due to SNe has been considered in the simulations based on the KMT models; in this case,  $H_2$  is continuously “painted” on the gas with no memory of the past conditions.

Finally, note that all our models for the formation of molecular hydrogen require the presence of dust (and hence metals) in order to catalyze the initial reactions. In fact, we do not follow  $H_2$  formation in the gas phase which is important only in very small objects (unresolved in our simulations) at early cosmic epochs (Abel et al. 1997, 1998). We therefore begin our simulations from pristine gas assuming a star formation law given by equation (14). These runs are stopped at  $z = 9$ , at which point we introduce a metallicity floor of  $Z_{\text{floor}} = 10^{-3} Z_{\odot}$  in the regions that are uncontaminated by prior star formation. The  $z = 9$  outputs are then used as the initial conditions for the runs that follow the distribution of  $H_2$  molecules from  $z = 9$  to  $z = 2$ . This procedure ensures that high-density, star forming clumps are enriched with metals more efficiently at early times, and also approximately accounts for the enrichment expected from unresolved Population-III star formation (see, e.g., Wolfe et al. 2005; Wise et al. 2012, for more detail).

### 3.4 Identification of galaxies and halos

In all simulation outputs, we identify gravitationally bound objects using the Amiga halo finder (AHF, Gill et al. 2004; Knollmann & Knebe 2009). Among other quantities, AHF returns the center of each halo, its virial mass,  $M_{200}$ , and corresponding virial radius,  $r_{200}$ . (Note that halo masses and radii are computed using all matter.) Within each halo, we define the stellar and gas mass of the central galaxy as that enclosed within a radius  $r_{\text{gal}} = 0.1 r_{200}$  (e.g. Scannapieco et al. 2012), which gives  $r_{\text{gal}} \simeq 12.6$  (physical) kpc for the largest galaxy in our simulations at  $z = 2$ .

In order to link galaxies between two consecutive outputs  $z_i < z_{i-1}$ , we consider a “descendant” halo identified at  $z_i$ , and search for all of its “progenitor” halos at  $z_{i-1}$ . Progenitors are defined as halos that have dark-matter particles in common with the descendant, the most massive of which we refer to as the “main progenitor”. The history of the main galaxy is tracked by studying the evolution of the material within 10 per cent of the virial radius of the main progenitor, which we compute in each simulation output.

## 4 RESULTS

### 4.1 Mass assembly

The mass-assembly history of the main halo in our DYN run is shown in Figure 3 (thick black line) over the redshift range  $z = 6$  to 2. The halo has a final dark-matter mass of  $1.8 \times 10^{12} M_{\odot}$  and exhibits a relatively quiescent recent formation history, with only two major-merging events that take place at  $z \sim 4.4$  and  $z \sim 3.5$ . At  $z = 2$  the halo contains hundreds of substructures, but more than 50 per cent of the stellar mass, and almost all of the molecular hydrogen, are located within the central galaxy (i.e. within 12.6 kpc from the halo center).

In Figure 3, we also show the mass build-up in the different components within  $r_{\text{gal}}$ : stars are shown using a dashed

Model	$M_*$ [ $10^{11} M_\odot$ ]	$M_{\text{gas}}^{\text{cold}}$ [ $10^{11} M_\odot$ ]	$M_{\text{gas}}^{\text{hot}}$ [ $10^{11} M_\odot$ ]	$M_{\text{H}_2}$ [ $10^{11} M_\odot$ ]	SFR [ $M_\odot \text{ yr}^{-1}$ ]	$\langle Z \rangle_M$ [ $Z_\odot$ ]	$\langle Z \rangle_*$ [ $Z_\odot$ ]	$\langle n_{\text{H}} \rangle_{20}^{\text{SFR}}$ [ $\text{cm}^{-3}$ ]	$\langle n_{\text{H}} \rangle_{50}^{\text{SFR}}$ [ $\text{cm}^{-3}$ ]	$\langle n_{\text{H}} \rangle_{80}^{\text{SFR}}$ [ $\text{cm}^{-3}$ ]
STD	1.15	0.35	0.27	0.34	66.5	0.92	0.72	10.2	29.7	83.7
DYN	1.06	0.34	0.16	0.17	59.3	0.97	0.72	1.7	7.3	39.4
KMT-UV	1.18	0.35	0.12	0.22	91.7	1.02	0.77	5.8	17.1	40.6
KMT-EQ	1.36	0.27	0.06	0.12	74.3	1.07	0.82	4.8	10.4	23.7

**Table 3.** Physical properties for the main galaxy at  $z = 2$ . The columns indicate the stellar, the cold ( $T < 10^4 \text{K}$ ), the hot ( $T > 10^4 \text{K}$ ) and the molecular gas mass, the star-formation rate (SFR), the mass-weighted gas and stellar metallicities, and 20th, 50th and 80th percentiles of the SFR-weighted gas density.

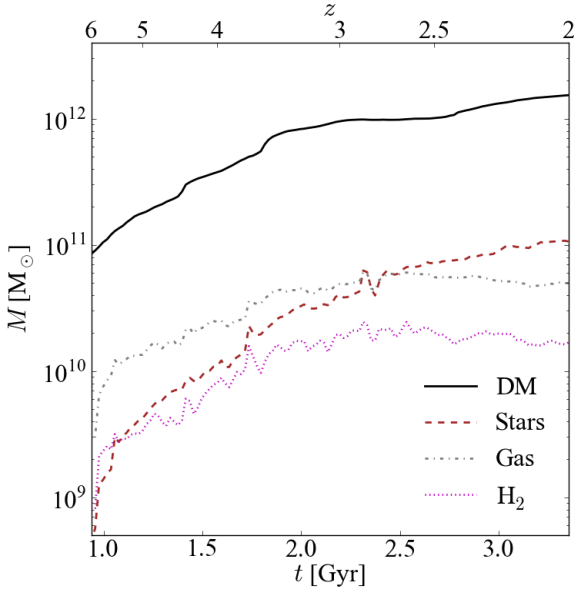


**Figure 3.** Assembly history of the main galaxy and its dark-matter halo in the DYN run. The solid (black) line shows the evolution of the dark-matter mass within  $r_{200}$ ; the mass of stars (brown dashed line), gas (gray dot-dashed line) and molecular hydrogen (magenta dotted line) measured within  $r_{\text{gal}}$  are also shown.

(red) line, total gas mass as a dot-dashed (grey) line, and the mass of molecular hydrogen as a dotted (magenta) line.

We can distinguish three main evolutionary epochs, each lasting for approximately 1 Gyr: one in which the main galaxy is assembled out of several small subgalactic objects (prior to  $z = 6$ ), followed by a phase of violent merging (particularly noticeable are the events at  $z \sim 3.7$  and  $z \sim 2.8$ ), and a final quiescent approach to  $z = 2$ . Note that the stellar mass steadily increases with time while the gas and  $\text{H}_2$  masses decrease slightly at late times. This is because the material used to form new stars is not efficiently replenished by accretion.

## 4.2 Global properties of the galaxies at $z = 2$

### 4.2.1 Comparison with observations

To facilitate a comparison between the different models, we list in Table 3 some key properties of the main galaxies in each simulation at  $z = 2$ , including their total stellar mass,  $M_*$ , as well as the gas masses in hot, cold and molecular components. We also list the star formation rate (SFR) and

the average gas and stellar metallicities. (All quantities have been measured within  $r_{\text{gal}}$ .)

Notice that, while the masses of stars and cold ( $T < 10^4 \text{K}$ ) gas are similar in all runs (i.e.  $M_* \simeq 1.1 \times 10^{11} M_\odot$ , and  $M_{\text{gas}}^{\text{cold}} \simeq 3 \times 10^{10} M_\odot$ ), the masses of molecular hydrogen,  $M_{\text{H}_2}$ , differ by more than a factor of 2.5 in different models. It is also worth noting that the mean gas and stellar metallicities tend to be slightly higher for the models in which SF is regulated by molecules. A number of aspects of the model contribute to this difference, including the total number of stars that are formed over time, as well as their ages and spatial distribution (see also Section 4.4).

In Figure 4 we compare several characteristics of our simulated galaxies in the  $z = 2$  output to observations of star forming galaxies at high-redshift. Outsized points in the left-hand panel plot the rotational velocity of the gas,  $v_{\text{rot}}$ , versus stellar mass for our simulations. Smaller symbols show the sample of Tacconi et al. (2010), which is divided into a high ( $\langle z \rangle = 2.3$ ) and a low redshift samples ( $\langle z \rangle = 1.2$ ). To make a meaningful comparison with this data – for which  $v_{\text{rot}}$  was determined from CO line emission – we compute the rotational velocity using only the cold gas component.

The star formation rate versus stellar mass is shown in the middle panel. Large and small symbols have the same meaning as before. All our model galaxies, independent of the assumed  $\text{H}_2$  and star formation laws, are forming stars at a similar rate, which is in good agreement with the observational dataset, as well as with the theoretically-determined star formation main sequence at  $z = 2$  given in Bouché et al. (2010).

Finally, the right panel shows the gas fraction, defined  $f_{\text{gas}} = M_{\text{gas}} / (M_{\text{gas}} + M_*)$ , versus galaxy stellar mass. Observationally,  $M_{\text{gas}}$  is determined from CO luminosity which is first converted into a molecular mass and then multiplied by a factor 1.36 to account for helium atoms that should be well-mixed with the molecules. This estimate coincides with the actual gas mass only if the contribution from atomic hydrogen is negligible.

In our simulations, this never holds true. Taking the DYN run at  $z = 2$  as an example, Table 3 shows that the cold atomic gas (H and He), the hot gas and the molecular hydrogen have all nearly identical masses (note that the table entry  $M_{\text{gas}}^{\text{cold}}$  includes  $M_{\text{H}_2}$ ). Therefore, in order to fairly compare the numerical results against the sample of Tacconi et al. (2010) we determine  $f_{\text{gas}}$  using the relationship  $M_{\text{gas}} = 1.36 M_{\text{H}_2}$ . These are shown as solid points in Figure 4. For comparison, we also show, using open symbols, the *total* gas fraction, which includes both atomic and molecular components.

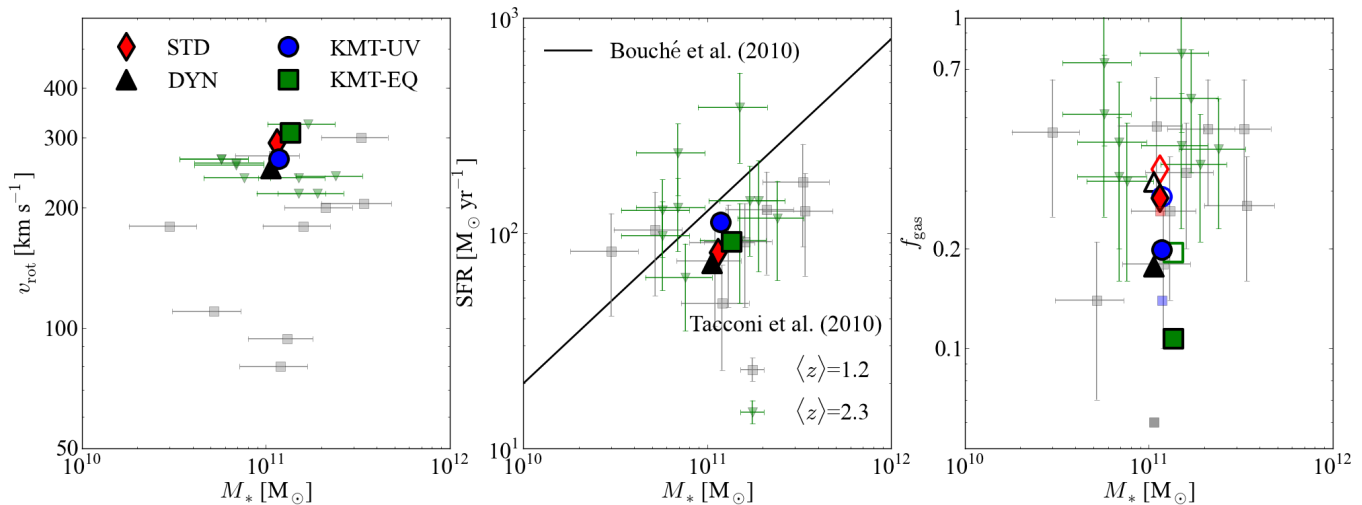


**Figure 4.** Gas rotational velocity (left panel), star formation rate (middle panel) and gas fraction (right panel) plotted versus the stellar mass of the main galaxy at  $z = 2$  for all runs. Heavy symbols correspond to our simulated galaxies, while small ones show the observed sample of Tacconi et al. (2010), which have been divided into low (gray squares) and high (green triangles) redshift subsamples. The solid black line in the middle panel is the galaxy SFR-main sequence at  $z = 2$  from Bouché et al. (2010). In the right-most panel, open symbols correspond to  $f_{\text{gas}}$  measured using the total gas mass, rather than the molecular component alone.

In general, the rotational velocities and SFRs of our simulated galaxies agree well with the observational dataset, particularly with the high-redshift sample. On the other hand,  $f_{\text{gas}}$ , when based on  $H_2$  alone, falls slightly below the majority of the observed data, particularly for the KMT-EQ model.

### 4.3 The internal structure of the galaxies at $z = 2$

#### 4.3.1 The resolved Kennicutt-Schmidt relation

It is useful to compare how the area-averaged star formation rate,  $\Sigma_{\text{SFR}}$ , and corresponding gas surface densities,  $\Sigma_{\text{gas}}$  and  $\Sigma_{\text{H}_2}$ , relate to each other in our simulations. To do this, we compute all surface densities using the face-on projection of the galaxies, and integrate the relevant quantities along a line-of-sight distance of 5 kpc above and below the mid-plane of the disc. In the orthogonal plane, we use square bins with a linear size of 720 pc, comparable to the resolution used in the observational study at  $z \sim 0$  by Leroy et al. (2008). In order to match observations that measure nebular emission lines ( $H\alpha$ , OII), which are sensitive to the light of young stars, we average the instantaneous star formation rate over the typical lifetime of OB stars, which we take to be 20 Myr. Note that we have verified that our results are robust with respect to small changes in the bin size, integration length, and stellar age.

Scatter plots of  $\Sigma_{\text{SFR}}$  versus  $\Sigma_{\text{gas}}$  and  $\Sigma_{\text{H}_2}$  are shown in Figure 5 for the STD and DYN simulations. The solid lines show the median  $\Sigma_{\text{gas}}$  (or  $\Sigma_{\text{H}_2}$ ) computed within bins of 0.5 dex in  $\Sigma_{\text{SFR}}$ , while the shaded regions indicate the 16th and 84th percentiles. The large filled symbols show the KS relation averaged over the entire galaxy. Power-law fits to observations of quiescent and starburst galaxies are indicated with dashed and dotted lines, respectively.

In both simulations, the amplitude and the slope of the resolved KS relation, expressed in terms of  $\Sigma_{\text{gas}}$ , are

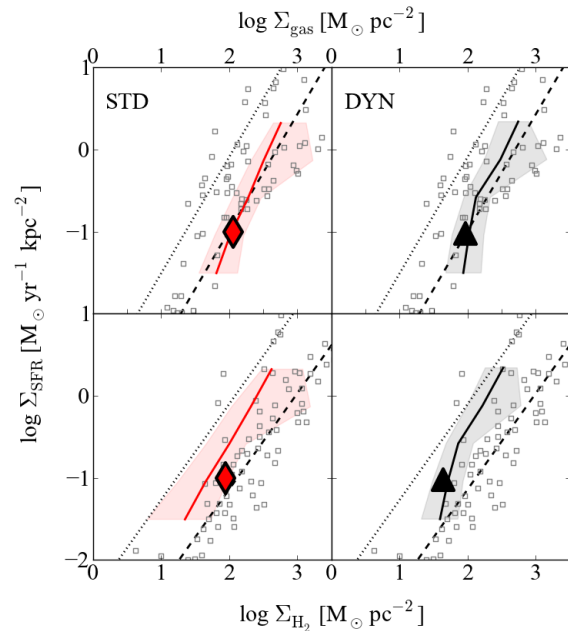


**Figure 5.** The Kennicutt-Schmidt relation for the total (*top panels*) and molecular gas column densities (*bottom panels*) for the STD (*left panels*) and DYN (*right panels*) models at  $z = 2$ . The dashed and dotted lines show the average observed relations for normal/quiescent galaxies and merging/starbursts systems, respectively, and gray squares the observed data for individual galaxies from Daddi et al. (2010) and Genzel et al. (2010). We have integrated the face-on gas and young stellar (i.e.  $t_s \leq 20$  Myr) mass distribution for a distance of 10 kpc centered on the mid-plane of the disc and used bins, in the transverse plane, of size 720 pc. The solid lines show the median gas (or molecular) surface density computed within bins of 0.5 dex in  $\Sigma_{\text{SFR}}$ , while shaded regions indicate the 16th and 84th percentiles. Outsized points in each panel show the KS-relation averaged over the entire area within  $r_{\text{gal}}$ .

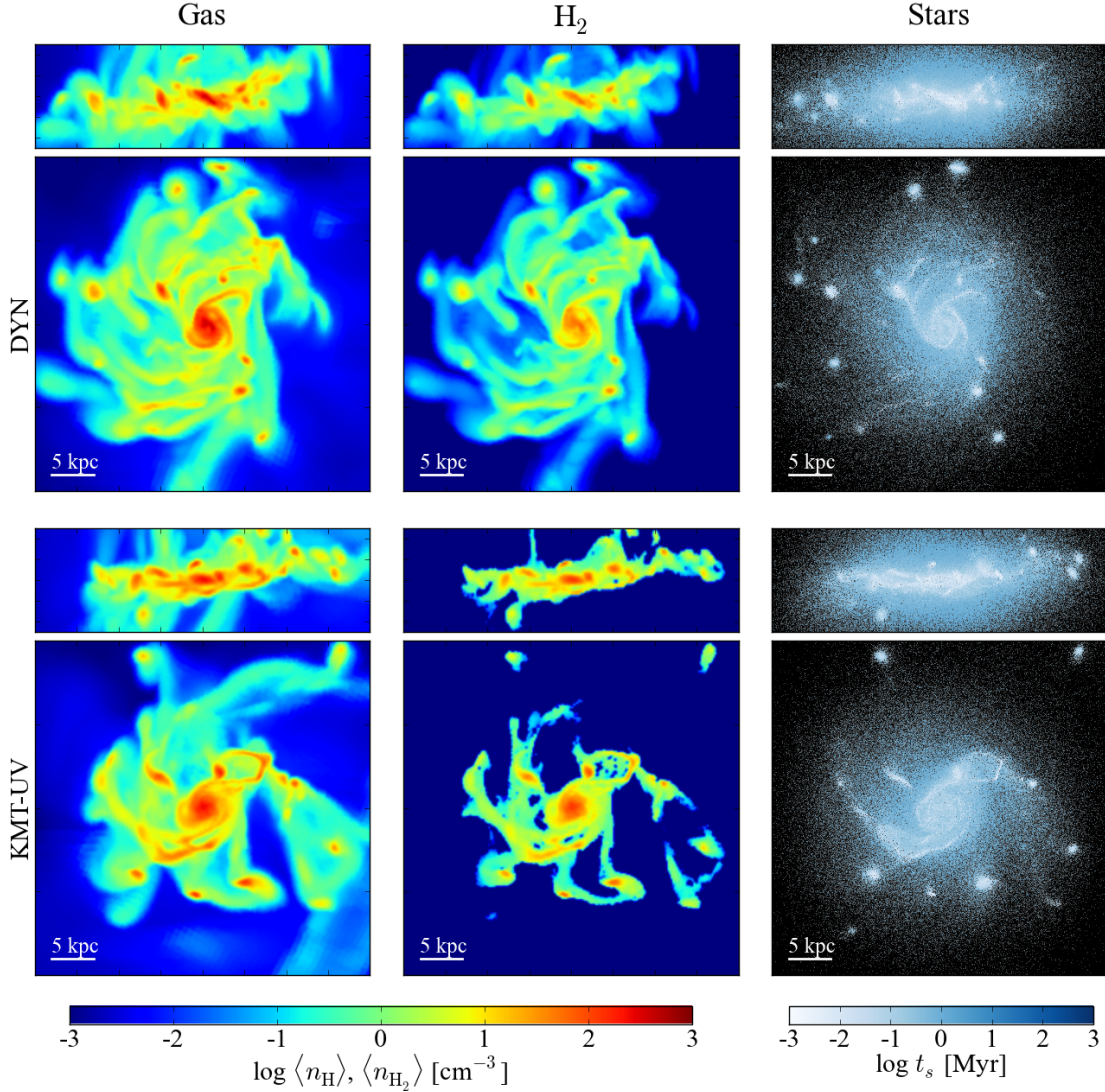


**Figure 6.** Face-on and edge-on views of the disc of the main galaxy in our DYN (top) and KMT-UV (bottom) runs at  $z = 2$  in a box of  $40 \times 40 \times 10$  kpc. From left to right, panels show the maximum hydrogen and  $\text{H}_2$  number densities along the line of sight, and the stellar distribution (color coded by stellar age), respectively.

in good agreement with the observed data for quiescent objects. Note that this happens by construction in the STD model: the parameters of the Schmidt law in equation (14) were tailored to achieve this. On the other hand, when using  $\Sigma_{\text{H}_2}$ , we find that the amplitude of the KS relation lies in between the observationally determined “starburst” and “normal disc” sequences. This is in good agreement with Kuhlen et al. (2012) and suggests that the star formation efficiency,  $\epsilon$ , should be slightly reduced in the molecule-regulated case. (Note that we obtain similar results for the other models and have therefore decided not to show those cases here.)

#### 4.3.2 The distribution of molecular hydrogen

Despite the fact that all models agree reasonably well with global observations of high-redshift galaxies, the detailed properties of the stellar, molecular and gaseous components in each simulation are rather different. For example, in Fig-

ure 6 we show the total hydrogen (left), the molecular hydrogen (center) and the stellar particle (right) distributions at  $z = 2$  for the main galaxy in two of our simulations. The top panels show the results for the DYN model while those on the bottom correspond to the KMT-UV run. The different assumptions used in these  $\text{H}_2$ -formation models are readily apparent in the  $\text{H}_2$  density distributions. Notice how including a sub-grid model for GMCs produces a more extended molecular disc as a result of more efficient formation of  $\text{H}_2$  in low-density gas. Nevertheless, the low densities in the outer regions contribute very little to the total  $\text{H}_2$ -mass budget in the DYN model.

Note also that, in regions where the gas density is high, the DYN run predicts less molecular hydrogen. This can be most easily seen in the central regions of the galaxy where both models predict a high total gas density but noticeably different densities of  $\text{H}_2$ . A more quantitative analysis is shown in Figure 7 where we compare the average  $\text{H}_2$  frac-

tion,  $f_{H_2}$  (computed as the ratio of the molecular to the total hydrogen surface densities), as a function of the projected radius in our different runs. The profiles for the chemical equilibrium models are similar: the  $H_2$  fraction reaches a maximum of  $\sim 95$  per cent within the innermost 1 kpc and steadily decreases toward larger radii, approaching  $f_{H_2} \approx 0$  at  $\sim 18$  kpc.

The DYN model, on the other hand, generates a very different radial  $H_2$  profile. At 18 kpc, for example, the molecular fraction is still  $\sim 25$  per cent, and molecular fractions below  $\sim 5$  per cent are reached only at radii  $\gtrsim 25$  kpc. This is consistent with the  $H_2$  abundances observed in the outskirts of nearby disc galaxies (Heyer et al. 2004; Leroy et al. 2008), which disagrees with the results obtained with the KMT models at  $z = 2$ . The extended  $H_2$  disc in the DYN model is a direct consequence of adopting a sub-grid density PDF for GMCs. Note, however, that the stellar disc follows an exponential profile with a scale length of  $\sim 4$  kpc in all  $H_2$ -regulated SF models.

Another striking difference in the radial  $H_2$  profiles between the KMT and DYN simulations is the central molecular fraction. Within the innermost  $\sim 2$  kpc, for example, the KMT models predict a  $H_2$  fraction of nearly 80 per cent. This is considerably higher than what is obtained in our DYN simulation, for which  $f_{H_2} \sim 0.4$  within the same radius. This may seem at odds with the results discussed in Section 2.2 where we showed that, under typical conditions, both KMT models require *higher* gas densities to become fully molecular. Figure 8 shows that this seemingly puzzling result is due to supernovae that, in our DYN model, destroy  $H_2$  which is unaffected in the KMT runs. In that figure, which is obtained from an output at  $z = 3.5$ , we compare the mean (mass-weighted)  $H_2$  fraction as a function of the cell density in the DYN and DYN-B simulations. Note that these two runs are identical in all aspects other than their treatment of  $H_2$  destruction by SNe (see Section 3.3). The suppression of  $f_{H_2}$  in the densest regions of the galaxy results in a total  $H_2$  mass that is nearly 30 per cent lower when  $H_2$  destruction by SNe is accounted for.

A key assumption of the  $H_2$ -models that we have considered here is that the abundance of dust traces the gas metallicity. Since  $H_2$  forms rapidly in dust-rich environments, this hypothesis has important consequences. In fact, at all epochs and in all simulations, we measure a tight correlation between the mass in metals,  $M_Z$ , and the  $H_2$  mass,  $M_{H_2}$ , at the cell level. For example, in the DYN model, the relation between  $M_Z$  and  $M_{H_2}$  can be accurately described by a power-law; the linear correlation coefficient in the log – log plane is  $\sim 0.99$ , and similar values are found for the KMT models, above a threshold mass of metals,  $M_Z \gtrsim 2 \times 10^3 M_\odot$ . The best-fit power-law parameters, however, evolve slowly with redshift. For example, in the DYN run, we find that  $M_{H_2} \propto M_Z^\alpha$  where  $\alpha$  grows smoothly from 0.96 to 1.07 in the redshift interval  $5 < z < 2$ . The constant of proportionality is  $\sim 30$  when masses are measured in units of  $M_\odot$ . After performing a careful calibration against the parameters of the sub-grid models, this tight correlation could be exploited to run computationally inexpensive simulations that link the abundance of molecular hydrogen directly to that of the metals.

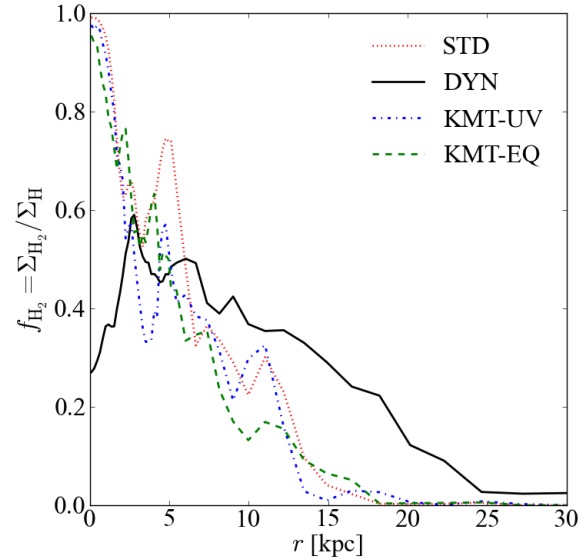


**Figure 7.** Molecular hydrogen fraction (computed as the ratio of the molecular to the total hydrogen surface densities in the face-on projection) as a function of projected radius  $r$  for all models at  $z = 2$ .

#### 4.4 Build-up of the molecular and stellar disc

In Figure 9, we show the time evolution of the mean mass-weighted  $H_2$  fraction as a function of the cell density for all of our simulations. We focus on four different epochs: an early time when the galaxy is assembling out of several smaller objects ( $z \sim 6$ ), two redshifts close to major merging events ( $z \sim 4.5$  and  $3.5$ ) and the final output at  $z = 2$ .

The KMT-EQ run shows a sharp  $H_2/H_I$  transition which progresses toward lower densities with time. This is expected since atomic gas is converted into molecules only if its surface density is greater than a critical value that is inversely proportional to the local metallicity. The shift of the transition scale therefore reflects the increasing metal content of the gas. In the KMT-UV and STD simulations, the critical surface density additionally depends on the interstellar UV field, which varies rapidly from cell to cell. This results in a broader transition of  $f_{H_2}$  with density as well as some irregularities.

Finally, the DYN run shows two peculiarities: first, an appreciable  $H_2$  fraction is found at much lower mean densities than in the KMT models, and second,  $\langle f_{H_2} \rangle$  stays well below unity, even in the densest regions. The first of these is due to the sub-grid density PDF adopted in the DYN model: the mean density of a cell is not representative of the regions in which  $H_2$  is formed. The latter is due to the combined effect of SNe explosions and star formation, which rapidly destroy or consume molecular hydrogen in the innermost/densest regions where star formation and SNe rates are highest.

In models that assume chemical equilibrium  $H_2$  abundance, even when molecules are used to form stars, they reform instantaneously: they are simply “painted” on the gas. On the other hand, our DYN simulations follow the time-dependent evolution of  $H_2$ , including its destruction due to star formation and SNe. When molecules are used to form stars, there is a recovery period over which they reform to

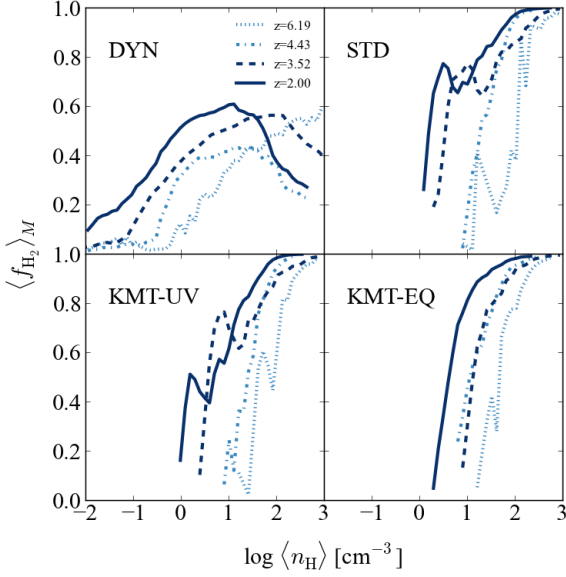


**Figure 8.** Distribution of the mass-weighted  $\text{H}_2$  fraction as a function of the cell density for the DYN (solid lines) and DYN-B (dashed lines) models at  $z = 3.5$ . The shaded regions indicate the 20th and 80th percentiles of the scatter. The top panel shows the total gas mass PDF.

their new abundance. This phenomenon slightly suppresses star formation in dense regions, since molecules must return to appreciable numbers once they have been used up by a previous star formation episode. Figure 8 clearly shows that  $\langle f_{\text{H}_2} \rangle$  does not reach unity in the densest regions even in the DYN-B simulation where SNe do not destroy  $\text{H}_2$ .

For the DYN model, both the shape and maximum value of the  $\langle f_{\text{H}_2} \rangle - \log \langle n_{\text{H}} \rangle$  relation correlate tightly with the SFR of the galaxy. When the latter is low,  $\langle f_{\text{H}_2} \rangle$  smoothly increases with  $\langle n_{\text{H}} \rangle$  (e.g. at  $z \sim 6.2$  when the SFR is  $10 M_{\odot} \text{ yr}^{-1}$ ) whereas a severe depletion of  $\text{H}_2$  at high densities is found during intense star formation episodes (e.g. at  $z \sim 4.4$  when the SFR is  $\sim 100 M_{\odot} \text{ yr}^{-1}$ ).

In the DYN model, even though the transition between atomic and molecular gas appears broad in terms of the cell densities, it becomes sharp when one considers the sub-grid densities used to compute  $\langle f_{\text{H}_2} \rangle$ . Dense clumps are indeed fully molecular in the DYN model; it is the volume average over the density PDF within the finite resolution elements which results in  $\langle f_{\text{H}_2} \rangle < 1$  when measured at the cell level. In Figure 10, we show how the intensity of LW radiation shifts the exact location of the transition at the sub-grid level. The critical density for  $\text{H}_2$  formation moves to higher densities in regions where  $\langle G \rangle$  is strong. The solid and the dashed lines (of equivalent color) highlight the impact of SNe and SF on the sub-grid density dependence of the  $\text{H}_2$  fraction. Solid lines show  $f_{\text{H}_2}$  averaged over *all* cells within  $r_{\text{gal}}$ , whereas dashed lines neglect cells with recent SF and SNe activity.

The evolution of the  $\text{H}_2$  (or total gas) profile in our simulations determines the structure of the stellar disc. In order to better assess the differences between our runs, we compare the radial distribution of stars at  $z = 2$  within their galaxy discs (i.e. within a cylinder of radius  $r \simeq 10$  kpc and height  $\pm 5$  kpc) in bins of stellar age. We choose the bins

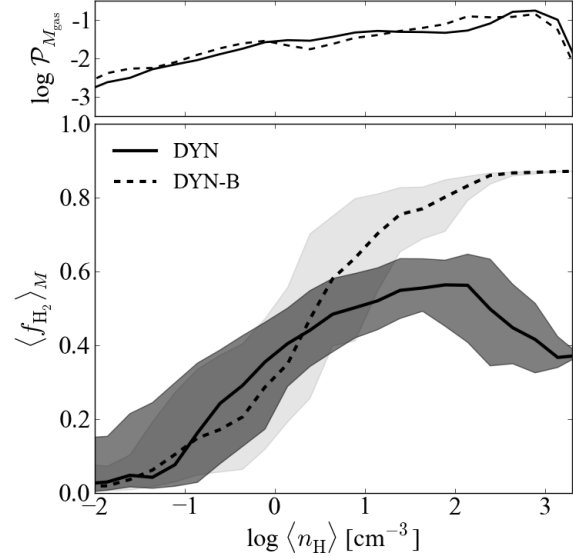


**Figure 9.** Distribution of the mass-weighted  $\text{H}_2$  fraction as a function of the cell density for each model. Different linestyles show results at four redshifts, as indicated in the legend.

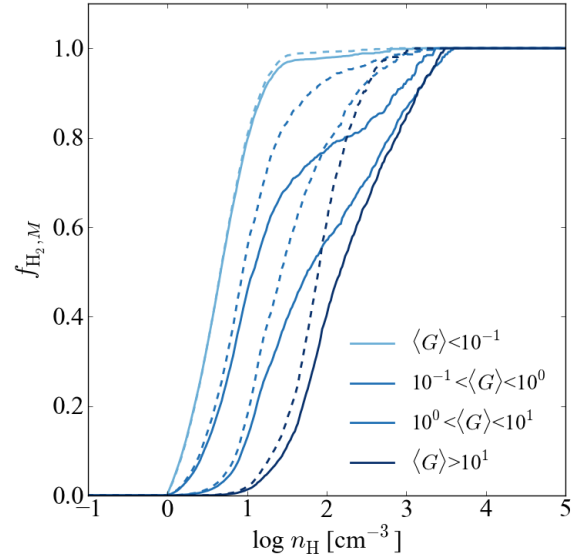


**Figure 10.** Distribution of the mass-weighted  $\text{H}_2$  fraction,  $f_{\text{H}_2, M}$ , as a function of the sub-grid density of total hydrogen,  $n_{\text{H}}$ , at  $z = 2$  for the DYN model. Solid lines include all cells within the galaxy radius, while dashed ones only account for cold gas (i.e. cells with active cooling and no recent  $\text{H}_2$  destruction due to SNe). Colors refer to different bins in the unshielded interstellar UV flux,  $\langle G \rangle$ .

so that, in the STD run, the stellar mass produced in each corresponds to one fifth of the total stellar mass at  $z = 2$ . The results are plotted in Figure 11 where later epochs are represented with lighter shades of blue. First, note that the STD and KMT-EQ runs have similar age distributions at each radius with an average of roughly 1.1 Gyr.

On the other hand, the KMT-UV simulation and (even

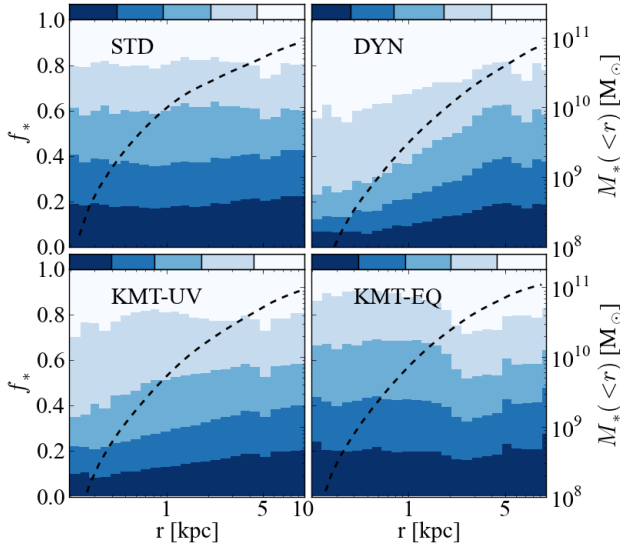


**Figure 11.** The radial distribution of stars within the galaxy disc (i.e. a cylinder of radius 10 kpc and height  $\pm 5$  kpc above and below the plane) at  $z = 2$ . Different colored regions indicate the fraction of stars as a function of radius sorted in five stellar age bins: [3.35, 1.76], [1.76, 1.36], [1.35, 0.94], [0.94, 0.45], [0.45, 0] Gyr (color-coded so that lighter shades of blue corresponds to later epochs). These bins are chosen so that, in the STD run, the stellar mass produced in each of them is equal to one fifth of the galaxy stellar mass at  $z = 2$ . The colored bars on top of each panel are scaled in size to match the fraction of stellar mass that is formed within each time bin. The cumulative stellar mass distribution (dashed lines) is also plotted for each model.

more so) the DYN run show significant differences in the age distribution of the stars lying in the innermost 5 kpc. These regions are populated by younger stars than in the STD case (the mean age of the stellar particles located at  $r < 1$  kpc is 0.75 Gyr in the DYN simulation and 0.9 Gyr in the KMT-UV). The total stellar mass within 1 kpc from the galaxy center at  $z = 2$  also varies significantly between the different models. In fact, we find values of  $M(r < 1 \text{ kpc}) = 1.1 \times 10^{10} M_\odot$  (STD),  $0.9 \times 10^{10} M_\odot$  (KMT-EQ),  $0.6 \times 10^{10} M_\odot$  (KMT-UV) and  $0.4 \times 10^{10} M_\odot$  (DYN). This phenomenon is due to the interstellar LW radiation which is stronger in the inner regions and suppresses  $H_2$  formation (for the DYN run SNe also contribute to the suppression of star formation in the central regions).

#### 4.5 “Failed” dwarf galaxies and early enrichment

It has recently been suggested that  $H_2$ -regulated star formation may result in a large population of “failed” dwarf-sized galaxies at  $z \gtrsim 2$  (Kuhlen et al. 2012, 2013). In spite of being gas rich, these objects never reached the critical surface density necessary to efficiently form  $H_2$  and therefore were not able to form an appreciable number of stars. It is important to stress, however, that the exact value of this density threshold depends strongly on the gas metallicity.

In order to track the  $H_2$  abundance in their simulations, Kuhlen et al. (2013) introduced a uniform metallicity floor at  $z = 10$ , neglecting possible star formation (and metal enrichment) at earlier epochs. This is different from our ap-

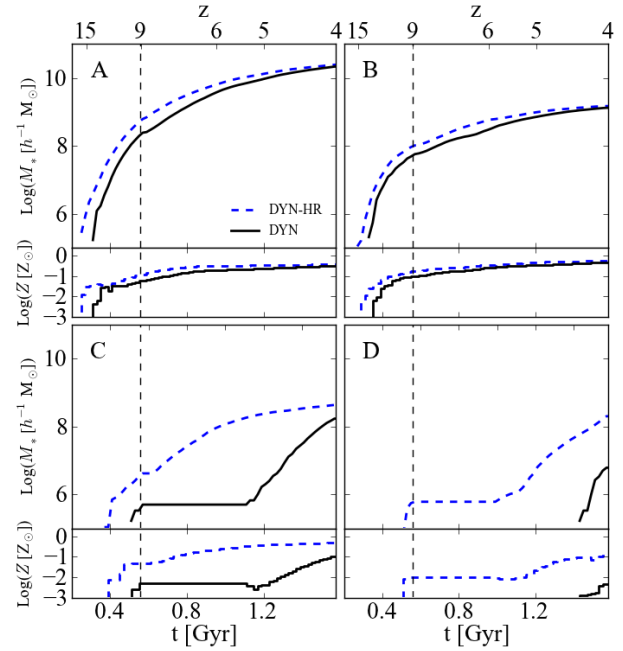


**Figure 12.** Mass-weighted stellar age distribution (*upper panels*) and average stellar metallicity (*lower panels*) for four different halos identified in the DYN (solid lines) and DYN-HR (dashed lines) runs at  $z = 4$ . Halo A is the main halo in our simulation; Halo B has a total mass  $M_{200} \sim 10.8 \times 10^{10} h^{-1} M_\odot$ ; and halos C and D have similar masses ( $M_{200} \simeq 6.2 \times 10^9 h^{-1} M_\odot$ ) but different enrichment histories. Prior to  $z = 9$  all models adopt a star formation law based on equation (14), and then switch to an  $H_2$  regulated model, equation (15). Note that the onset of efficient star formation at redshifts  $z < 9$  depends sensitively on the previous metal enrichment of the halo, which is influenced by both resolution as well as the unique assembly history of each object.

proach in which stars are formed based on a gas-regulated law (equation (14)) until  $z = 9$ , at which point we introduce a uniform metallicity floor in all *uncontaminated* regions (see Section 3.3). This procedure results in a higher metal abundance in high-density regions where star formation was able to take place prior to  $z = 9$ .

Models of early enrichment indicate that there may already be galaxies with nearly solar metallicity at  $z \sim 9 - 10$  (e.g. Wise et al. 2012), and the ( $z = 9$ ) initial conditions for our simulations that include  $H_2$  are in qualitative agreement with these expectations. Moreover, in our approach, halos with different masses and accretion histories contain different amounts of metals at the point of transitioning to the  $H_2$ -based star formation models.

It is therefore worthwhile investigating how the metal distribution at  $z = 9$  alters the star formation histories of galaxies hosted by dark-matter halos located in the high-resolution region of our simulations. To do this, we first cross-match the dark-matter halos between the DYN and DYN-HR simulations and then compare their star formation histories. Note that this is not able to distinguish the effects of a resolution-dependent metallicity from the benefits of resolving higher gas densities. We have checked, however, that the increase in density contributes only partially to the differences that we are going to describe.

For simplicity, we focus on four particular objects identified in each run at  $z = 4$ : our main halo (A), a second halo (B) with a total mass of  $M_{200} \sim 10.8 \times 10^{10} h^{-1} M_{\odot}$ , and two smaller halos (C and D) of similar mass,  $M_{200} \simeq 6.2 \times 10^9 h^{-1} M_{\odot}$ , but different enrichment histories which we quantify by measuring the average metallicity of the stars within  $r_{200}$  that formed at  $z > 9$ ,  $Z_{>9}$ . Figure 12 shows the stellar-mass build-up and the evolution of the mean stellar metallicity for each of these four halos at both resolutions. Results obtained from our DYN-HR run are shown using dashed lines, whereas solid lines are used for DYN.

Halos A and B have already built up a considerable stellar mass by  $z = 9$ . The enrichment associated with this early star formation raised the average metallicities of these halos to  $Z_{>9} \simeq 10^{-1} Z_{\odot}$ , independent of resolution. As a result, neither show a significant suppression of star formation at  $z < 9$  (their stellar-mass build-up increases smoothly with time in both runs). Conversely, halo C has a mean stellar metallicity that differs by nearly an order of magnitude between the low and high resolution runs. This results from the fact that, at higher resolutions, the gas reaches higher densities and therefore forms stars more efficiently. Note that the lack of metals leads to a clear suppression of star formation lasting for  $\sim 100 - 200$  Myr after  $z = 9$  in the low resolution run. This “delay” essentially disappears in the DYN-HR simulation, where  $Z_{>9}$  for this object is an order of magnitude larger.

An even more extreme example is given by halo D. This object does not form any stars prior to  $z = 9$  in the low-resolution simulation; its metallicity at that point is thus equal to the value of our metallicity floor,  $10^{-3} Z_{\odot}$ . In the DYN-HR run, on the other hand, halo D has already formed a small number of stars prior to  $z = 9$ , resulting in a mean metallicity that is roughly an order of magnitude larger than in the lower-resolution case. This change in metallicity significantly affects the timescale needed to produce sufficient molecules to efficiently fuel star formation. In the DYN-HR run, for example, the onset of star formation occurs nearly  $\Delta t = 500$  Myr after  $z = 9$ , while  $\Delta t = 1$  Gyr in the low-resolution run.

In summary, failed galaxies at a given redshift might become bright when simulated at higher resolution, or with realistic pre-enrichment scenarios. In fact, the fraction of bright halos (i.e. halos that contain at least  $10^8 h^{-1} M_{\odot}$  of stars) with  $M_{200} \lesssim 10^{10} h^{-1} M_{\odot}$  at  $z = 4$  nearly doubles when the linear resolution is increased by a factor of 2. Based on this, we conclude that combining realistic models of early metal enrichment in protogalactic regions with high-resolution simulations is needed in order to make trustworthy predictions regarding the abundance of dark galaxies at high-redshift.

## 5 CONCLUSIONS

We have presented a sub-grid model for tracking the non-equilibrium abundance of molecular hydrogen in cosmological simulations of galaxy formation. The novelty of the model is that it phenomenologically accounts for the distribution of unresolved sub-grid densities determined from observations and simulations of the turbulent ISM.

We have implemented our model in the RAMSES code in order to run simulations that track the evolution of the  $H_2$  content of a massive galaxy at  $z = 2$ , and to study the imprint of  $H_2$ -regulated star formation. In order to better understand what determines the properties of a galaxy, we ran a suite of simulations of the same dark matter halo, each with a different prescription for computing the  $H_2$  distribution. In the runs where  $H_2$  is calculated explicitly, star formation was regulated by the local  $H_2$  abundance, while, for another, we adopted the traditional Schmidt law based on the total gas density. Our main findings can be summarized as follows:

(i) The main galaxy in our simulations has similar global properties at  $z = 2$ , regardless of the assumed star formation law. This is mainly due to the fact that the average metallicity of the gas in its dominant progenitors is already  $\sim 10^{-1} Z_{\odot}$  at  $z = 9$ . As a result, subsequent  $H_2$  formation is rapid, mitigating any subtle differences in the  $H_2$  models and resulting in very similar star formation rates independent of whether stars form from atomic or molecular gas.

(ii) However, the detailed properties of the  $H_2$  distribution are strongly influenced by the different sub-grid prescriptions for  $H_2$  formation. The total  $H_2$  mass of the galaxy, for example, differs by as much as a factor of 2.5 between the different models. Moreover, our time-dependent model produces a galaxy with an extended molecular disc, while the equilibrium prescriptions produce a steep decline of the  $H_2$  fraction at large radii. This is a direct result of assuming a sub-grid density distribution, which allows  $H_2$  to form more easily in low density cells.

(iii) If molecular hydrogen is efficiently destroyed by supernovae, then the resulting  $H_2$  fraction decreases in the innermost/densest regions of the galaxy (within approximately 2-3 kpc from the galactic center). Because star formation and SNa rates are highest in the central regions, this depression of  $f_{H_2}$  is long-lived, with  $H_2$  fractions rarely exceeding  $\sim 40$  per cent. Note, however, that the density of  $H_2$  rises continuously toward the central regions.

(iv) Regardless of the  $H_2$  model, the molecular mass in a cell scales linearly with the that of the metals (above a model-dependent threshold density). This is a consequence of assuming that dust traces the metals in the simulations. The slope of the relation, however, evolves slightly with redshift and from model to model, making predictions of the  $H_2$  abundances based on metals alone challenging.

(v) Contrary to the assumption that gas is fully molecular in high-redshift galaxies (commonly used to interpret CO observations, e.g. Tacconi et al. (2010); Genzel et al. (2010); Magnelli et al. (2013)), the atomic gas fraction in our simulated galaxy is comparable to the molecular contribution, independent of the  $H_2$  formation model.

(vi) When a molecule-regulated star formation law is adopted, the star formation history of dwarf-sized galaxies is strongly influenced by early metal enrichment and numerical resolution. This is due to the fact that metal poor halos require more time to build up a substantial molecular reservoir that can be used as fuel for star formation. This hinders the interpretation of simulations that aim to assess the impact of  $H_2$ -regulated star formation on low mass galaxy formation and stress the importance of properly modeling the enrichment history of individual halos.

Although our non-equilibrium  $H_2$  model represents a significant improvement over previous methods, many challenges still remain. For instance, we have assumed that the sub-grid density PDF of GMCs can be accurately described by a log-normal. This is based on several observations of molecular clouds which, in some cases, show high-density tails in star forming regions (e.g. Kainulainen et al. 2009; Schneider et al. 2013). Several complex physical phenomena like energy injection, turbulence, gravity and external compression influence the density structure of molecular clouds. Yet, numerical studies of the ISM have shown that the log-normal model is a good approximation when an isothermal gas flow is supersonically turbulent (e.g. Vazquez-Semadeni 1994; Glover & Mac Low 2007a,b; Federrath et al. 2009; Federrath & Klessen 2013). Power-law tails in the high-density regime form under the presence of self-gravity (which generates dense cores and super-critical filaments). Non-isothermal turbulence can also increase the occurrence of dense clumps. None the less, these uncertainties are likely sub-dominant to those associated with modeling the effects of SNa feedback on GMCs, which must be tackled with small-scale simulations of the ISM.

In addition, we have set the dispersion of the log-normal density distribution to be  $\sigma \simeq 1.5$ , consistent with a constant clumping factor  $C_\rho = 10$ . This choice was motivated by theoretical work that relates local density enhancements to the three-dimensional rms Mach number,  $\mathcal{M}$ , with values of  $\mathcal{M} \sim 5.5$  (e.g. Padoan et al. 1997; Ostriker et al. 2001; Price et al. 2011). Moreover, the same value for the clumping factor has been adopted in the literature to best match the  $H_2$  content in observations and simulations (e.g. Gnedin et al. 2009; Christensen et al. 2012). However, observations of GMCs have revealed substantial variations in the Mach number (Schneider et al. 2013). In future implementations, the realism of our model can be improved adjusting the clumping factor (as well as the PDF of the sub-grid density) in cells with different mean densities and temperatures. From the technical point of view, this is straightforward to do: the difficulty lies in linking the mean properties of a cell to the sub-grid parameters that regulate the density PDF. One intriguing possibility could be to implement a simplified description of supersonic turbulence along the lines of that proposed by Teyssier et al. (2013). We plan to return to these issues in future work.

## ACKNOWLEDGEMENTS

We thank Romain Teyssier and Tom Abel for helpful discussions and acknowledge support from Mark Labadens for the software PyMSES and from Oliver Hahn for the MUSIC code. This work was supported by the Deutsche Forschungsgemeinschaft (DFG) through the project SFB 956 *Conditions and Impact of Star Formation*, sub-project C4. MT was supported through a stipend from the International Max Planck Research School (IMPRS) for Astronomy and Astrophysics in Bonn. We acknowledge that the results of this research have been achieved using the PRACE-2IP project (FP7 RI-283493) resources HeCTOR based in the UK at the UK National Supercomputing Service and the Abel Computing Cluster based in Norway at the University of Oslo.

## REFERENCES

- Abel T., Anninos P., Norman M. L., Zhang Y., 1998, ApJ, 508, 518
- Abel T., Anninos P., Zhang Y., Norman M. L., 1997, NEWA, 2, 181
- Agertz O., Kravtsov A. V., Leitner S. N., Gnedin N. Y., 2013, ApJ, 770, 25
- Bigiel F., Leroy A., Walter F., Brinks E., de Blok W. J. G., Madore B., Thornley M. D., 2008, AJ, 136, 2846
- Bouché N., Dekel A., Genzel R., Genel S., Cresci G., Förster Schreiber N. M., Shapiro K. L., Davies R. I., Tacconi L., 2010, ApJ, 718, 1001
- Burke J. R., Hollenbach D. J., 1983, ApJ, 265, 223
- Carilli C. L., Walter F., 2013, ARA&A, 51, 105
- Cazaux S., Spaans M., 2004, ApJ, 611, 40
- Cazaux S., Spaans M., 2009, A&A, 496, 365
- Christensen C., Quinn T., Governato F., Stilp A., Shen S., Wadsley J., 2012, MNRAS, 425, 3058
- Daddi E., Elbaz D., Walter F., Bournaud F., Salmi F., Carilli C., Dannerbauer H., Dickinson M., Monaco P., Riechers D., 2010, ApJL, 714, L118
- Dobbs C. L., Krumholz M. R., Ballesteros-Paredes J., Bolatto A. D., Fukui Y., Heyer M., Mac Low M.-M., Ostriker E. C., Vázquez-Semadeni E., 2013, ArXiv e-prints
- Draine B. T., Bertoldi F., 1996, ApJ, 468, 269
- Federrath C., Klessen R. S., 2013, ApJ, 763, 51
- Federrath C., Klessen R. S., Schmidt W., 2009, ApJ, 692, 364
- Feldmann R., Gnedin N. Y., Kravtsov A. V., 2011, ApJ, 732, 115
- Genzel R., Tacconi L. J., Gracia-Carpio J., Sternberg A., Cooper M. C., Shapiro K., Bolatto A., Bouché N., Bournaud F., Burkert A., Combes F., Comerford J., Cox P., Davis M., Schreiber N. M. F., 2010, MNRAS, 407, 2091
- Gill S. P. D., Knebe A., Gibson B. K., 2004, MNRAS, 351, 399
- Glover S. C. O., Clark P. C., 2012, MNRAS, 426, 377
- Glover S. C. O., Mac Low M.-M., 2007a, ApJS, 169, 239
- Glover S. C. O., Mac Low M.-M., 2007b, ApJ, 659, 1317
- Gnedin N. Y., Tassis K., Kravtsov A. V., 2009, ApJ, 697, 55
- Haardt F., Madau P., 2012, ApJ, 746, 125
- Hahn O., Abel T., 2011, MNRAS, 415, 2101
- Heyer M. H., Corbelli E., Schneider S. E., Young J. S., 2004, ApJ, 602, 723
- Hopkins P. F., Kereš D., Murray N., Quataert E., Hernquist L., 2012, MNRAS, 427, 968
- Kainulainen J., Beuther H., Henning T., Plume R., 2009, A&A, 508, L35
- Kennicutt Jr. R. C., 1989, ApJ, 344, 685
- Kennicutt Jr. R. C., 1998, ApJ, 498, 541
- Kennicutt Jr. R. C., Calzetti D., Walter F., Helou G., Hollenbach D. J., Armus L., Bendo G., 2007, ApJ, 671, 333
- Knollmann S. R., Knebe A., 2009, ApJS, 182, 608
- Komatsu E., Smith K. M., Dunkley J., Bennett C. L., Gold B., Hinshaw G., Jarosik N., Larson D., Nolte M. R., Page L., Spergel D. N., Halpern M., Hill R. S., 2011, ApJS, 192, 18
- Kroupa P., 2001, MNRAS, 322, 231
- Krumholz M. R., 2012, ApJ, 759, 9
- Krumholz M. R., Gnedin N. Y., 2011, ApJ, 729, 36

- Krumholz M. R., McKee C. F., Tumlinson J., 2008, *ApJ*, 689, 865
- Krumholz M. R., McKee C. F., Tumlinson J., 2009, *ApJ*, 693, 216
- Kuhlen M., Krumholz M. R., Madau P., Smith B. D., Wise J., 2012, *ApJ*, 749, 36
- Kuhlen M., Madau P., Krumholz M., 2013, *ArXiv e-prints*
- Leitherer C., Schaerer D., Goldader J. D., González Delgado R. M., Robert C., Kune D. F., de Mello D. F., Devost D., Heckman T. M., 1999, *ApJS*, 123, 3
- Leroy A. K., Walter F., Brinks E., Bigiel F., de Blok W. J. G., Madore B., Thornley M. D., 2008, *AJ*, 136, 2782
- Magnelli B., Popesso P., Berta S., 2013, *A&A*, 553, A132
- McKee C. F., Krumholz M. R., 2010, *ApJ*, 709, 308
- Micic M., Glover S. C. O., Federrath C., Klessen R. S., 2012, *MNRAS*, 421, 2531
- Ostriker E. C., Stone J. M., Gammie C. F., 2001, *ApJ*, 546, 980
- Padoan P., Nordlund A., Jones B. J. T., 1997, *MNRAS*, 288, 145
- Pelupessy F. I., Papadopoulos P. P., van der Werf P., 2006, *ApJ*, 645, 1024
- Pirogov L. E., 2009, *Astronomy Reports*, 53, 1127
- Price D. J., Federrath C., Brunt C. M., 2011, *ApJL*, 727, L21
- Rogers H., Pittard J. M., 2013, *MNRAS*, 431, 1337
- Scannapieco C., Wadepuhl M., Parry O. H., Navarro J. F., Jenkins A., Springel V., Teyssier R., Carlson E., Couchman H. M. P., Crain R. A., Dalla Vecchia C., 2012, *MNRAS*, 423, 1726
- Schmidt M., 1959, *ApJ*, 129, 243
- Schneider N., André P., Könyves V., Bontemps S., Motte F., Federrath C., Ward-Thompson D., Arzoumanian D., 2013, *ApJL*, 766, L17
- Stinson G., Seth A., Katz N., Wadsley J., Governato F., Quinn T., 2006, *MNRAS*, 373, 1074
- Tacconi L. J., Genzel R., Neri R., Cox P., Cooper M. C., Shapiro K., Bolatto A., Bouché N., Bournaud F., Burkert A., Combes F., Comerford J., Davis M., Schreiber N. M. F., 2010, *Nature*, 463, 781
- Tajiri Y., Umemura M., 1998, *ApJ*, 502, 59
- Teyssier R., 2002, *A&A*, 385, 337
- Teyssier R., Chapon D., Bournaud F., 2010, *ApJL*, 720, L149
- Teyssier R., Pontzen A., Dubois Y., Read J. I., 2013, *MNRAS*, 429, 3068
- Tielens A. G. G. M., Hollenbach D., 1985, *ApJ*, 291, 722
- Truelove J. K., Klein R. I., McKee C. F., Holliman II J. H., Howell L. H., Greenough J. A., 1997, *ApJL*, 489, L179
- Vazquez-Semadeni E., 1994, *ApJ*, 423, 681
- Wise J. H., Turk M. J., Norman M. L., Abel T., 2012, *ApJ*, 745, 50
- Wolfe A. M., Gawiser E., Prochaska J. X., 2005, *ARA&A*, 43, 861

function (IMF) – to compute the luminosity in the LW band,  $L_{\text{LW}}(t_s)$ , as a function of stellar age,  $t_s$ . We then propagate this radiation up to a maximum distance assuming that the gas is optically thin. For each spatial location, we only consider sources of radiation that lie within an oct, i.e. a collection of 8 cells at the highest level of refinement. Therefore the corresponding UV flux is:

$$G(t) = \frac{1}{G_0} \frac{\sum_{i \in \text{oct}} L_{\text{LW}}(t - t_{s,i})}{\alpha 4\pi (\Delta x)^2}, \quad (\text{A1})$$

where  $t$  is the time elapsed in the simulation and  $\Delta x$  indicates the size of a resolution element. The factor  $\alpha \simeq 6.3$  gives the correct average flux at the center of a cell when stars are randomly distributed (with uniform density) within an oct. This coefficient has been measured with a Monte Carlo method. In our simulations,  $\Delta x \simeq 65 - 130 h^{-1} \text{ pc}$  and is comparable with the typical size of GMCs.

## APPENDIX A: INTERSTELLAR UV FIELD

Each star particle in our simulations represents a simple stellar population. We use the STARBURST99 templates (Leitherer et al. 1999) – with a Kroupa (2001) initial mass